

1 Optimizing WRF as a regional climate Downscaling Tool for
2 Hydro-climatological Applications in the Eastern Nile Basin

3
4 Mahmoud Osman^{a*}

5 George Zittis^b

6 Mohammed AbouElHaggag^a

7 Ahmad W. Abdeldayem^a

8 Jos Lelieveld^{b,c}

9
10 ^a Faculty of Engineering, Cairo University, Giza, Egypt.

11 E-mail: mosman@cu.edu.eg; mosman7@jhu.edu; Tel. +1(970)412-7545

12
13 ^b The Cyprus Institute, Nicosia, Cyprus.

14 ^c Max Planck Institute for Chemistry, Mainz, Germany.

15
16
17 _____
18 This study contributes to the development of an integrated hydro-climate model for the EN basin for
19 the impact assessment of the Nile inflow at Aswan by configuring a RCM using WRF to downscale
20 ERA-Interim reanalysis data from 1980 to 2009 and correct the resulted model bias.

21
22 **Keywords:**

23 Dynamic downscaling; Bias correction; Eastern Nile Basin; WRF; Precipitation patterns

24 **1. Abstract:**

25 Most of the Nile water inflow at High Aswan Dam (HAD), Egypt, originates from the
26 Ethiopian plateau, providing the main source of water for the Eastern Nile (EN) basin. The
27 Weather Research and Forecasting (WRF) model using ARW (Advanced Research WRF)
28 dynamical core is configured for a domain centered over the EN with a parent domain
29 defined for the Middle East – North Africa (MENA). WRF physics parameterization
30 sensitivity experiments are carried out to select an optimum combination of physics schemes
31 to reproduce observed climate conditions. The model skill is also examined by downscaling
32 the ERA-Interim reanalysis dataset from 1980 to 2009 over the EN basin domain. The WRF
33 performance is assessed using gridded observational datasets for precipitation, temperature
34 and evapotranspiration. The model is tested for four different configurations in two-year
35 simulations to determine the optimal combination of physics parameterizations prior to the
36 30-year downscaling experiment. The results indicate accurately modelled temperature and
37 evapotranspiration fields, however, with significant positive precipitation biases, especially
38 over the highlands. The bias-corrected precipitation data is coupled to the semi-distributed
39 hydrological rainfall-runoff model (SWAT) model, previously configured for the Baro-
40 Akobo-Sobat sub-basin. The simulated flow hydrograph based on bias-corrected WRF
41 simulations yields high statistical significance for the observed flow hydrographs. Results
42 indicate that the simulated precipitation fields from WRF should be subject to bias correction
43 prior to use in hydrological models especially for impact studies.

44 **2. Introduction**

45 Throughout the last three decades, global and regional climate models have been developed
46 and widely utilized to project future climate conditions, and to help better understand the
47 present and past climate [6,10,26,31]. Dynamic downscaling techniques can be applied to
48 bring global-scale projections down to a regional level where the output of general circulation
49 models (GCMs) provides the initial and boundary conditions. Considerable computing
50 resources are involved, where high resolution climate scenarios provided by regional climate
51 models (RCMs) allow for a more precise description of topographic forcing due to orography,
52 land-sea contrasts and land-use characteristics [11,17,20]. In this study, we use the Weather
53 Research and Forecasting Model (WRF) version 3.5, which is used by more than 30,000
54 researchers in excess of 150 countries, and allows researchers to generate atmospheric
55 simulations based on real data (observations, reanalysis) or idealized conditions
56 (<http://www.wrf-model.org>).

57 Assessments of the future climate in the Eastern Nile Basin (EN) basin are still limited and
58 the level of understanding of future climate behavior is not yet clear to the different decision
59 makers and stakeholders in the EN. This is mainly because of the complexity of carrying out
60 representative climate studies. The complexity and chaotic nature of the climate system
61 suggest that future climate conditions cannot be represented by simply extrapolating past
62 climate conditions. Instead, mathematical representations of the Earth's climate system
63 through high resolution RCM the accounts for the region's climatic physics.

64 This study pursues a high-resolution RCM for the EN basin that is configured and bias
65 corrected based on a 30-year simulation period (from 1980 to 2009) and serving hydro-
66 climatological applications.

67 There is a paucity in the relevant research studies that assess the performance of the WRF
68 model over the Nile basin and specifically over the EN basin. Few studies [1,5,14,37,44]

69 focused on the impacts of climate change on the hydrology at different regions in the Nile
70 basin hydrology and Lake Victoria basin using WRF dynamic downscaling and statistical
71 downscaling techniques. The objective of our study is to fill the gap in the EN basin region
72 by optimizing the WRF for dynamic downscaling instead of using the classical statistical
73 downscaling techniques as well as studying the generated bias from the model
74 hydrodynamics. The results of the study are expected to be used in future dynamic
75 downscaling of climate models for hydro-climatological applications using pre-configured
76 WRF model. The model is configured for the simulations using the WRF-ARW (Advanced
77 Research WRF) dynamical core developed at the National Center for Atmospheric Research
78 (NCAR) [38].

79

80 **3. Materials and Methods**

81 **2.1. Region of Study**

82 The EN hydrologic boundaries extend from the Ethiopian Highlands ($\sim 3^{\circ}\text{N}$) in the south to
83 the High Aswan Dam (HAD) in the North ($\sim 24^{\circ}\text{N}$) and from the west of Sudan ($\sim 26^{\circ}\text{E}$) to
84 the Gulf of Aden ($\sim 42^{\circ}\text{E}$) as shown in Figure 1. Elevations in the EN basin range from 0 to
85 4,300 meters above mean sea level. About 5% of the basin lies in very low elevated areas
86 while most of the EN (around 70%) is situated within the range of 300 - 600 m. Another 20%
87 is between 600 - 2000 m and the remaining 5% is associated with very steep slopes (around
88 2000 m - 4300 m) [41]. Ethiopia has a general elevation ranging from 1,500 to 3,000 m and
89 the plateau height exceeds 4,000 m. A key land feature in Ethiopia is Lake Tana, created by
90 volcanic activity, at a height of 1,785 m. In Sudan, elevations vary between 170 m and 1,475
91 m whereas in South Sudan, elevation ranges from 380 m to 2,885 m [3,34,37,41]

92 The EN is divided into five sub-basins that include the Main Nile, the Baro-Akobo-
93 Sobat,-White Nile, the Abay-Blue Nile, and the Tekeze-Atbara-Setite. The Abay-Blue Nile
94 and the Main Nile region host nearly 82% of the total population [13,37].

95 Precipitation over the Nile basin increases from the north to the south (with elevation)
96 with values up to 1,600 mm/year over the Ethiopian highlands, which is mainly governed by
97 the interaction with the basin topography and the Inter-Tropical Convergence Zone
98 movement [32,41].

99 **2.2. Methodology**

100 The methodology applied for hydro-climatic simulations and dynamical climate
101 downscaling over the EN basin is summarized in the flow chart of Figure 2. The regional
102 climate modeling is carried out using version 3.5 of the WRF model over a domain covering
103 the Middle East and North Africa (MENA) including the EN region. Climate downscaling is
104 performed by forcing the WRF model with initial and boundary conditions from the
105 European Centre for Medium-Range Weather Forecast (ECMWF) ERA-Interim reanalysis
106 dataset [4], in order to (a) select the suitable combination of physics parameterizations and
107 (b) investigate the model skill in reproducing the past and present climate conditions. The
108 model is configured as sub-domain (nest) in the Coordinated Regional Climate Downscaling
109 Experiment (CORDEX)-MENA domain, encompassing 185 x 250 horizontal grid points
110 (~10km grid resolution) and 30 vertical grid levels as shown in Figure 3. The integration
111 timestep is set to 240 seconds for the MENA parent domain computations and 1:5 as parent to
112 nest timestep ratio which is the same ratio used for nesting the EN domain. The spin-up time
113 is set to seven months after sensitivity analysis to model for different spin-up periods.

114 Because the CORDEX domain is large and parts of it are out of context for the EN
115 region we focus our evaluation only on the high-resolution nest and the 12 sub-domains listed
116 in Table 2 that represent the individual watersheds of the EN and cover different climatic

117 zones up to the High Aswan Dam. The selected regions are equally sized as boxes of
 118 dimensions 2° by 2° represented in Figure 1. Each of them covers approximately 484 grid
 119 points at the EN domain selected resolution.

120 **2.3 Sensitivity to Physics Parameterization**

121 Based on previous study of the CORDEX MENA domain [45,46] and following other
 122 physics sensitivity studies [7,15,18,19,24,27,28,33,36,39], four physics combinations,
 123 commonly used for regional climate simulations, are used to test the model sensitivity
 124 towards different parameterization schemes (Table 1). The physics representations were
 125 tested for precipitation and temperature over two years of extreme different precipitation
 126 regimes over the Nile basin; 1999 as a wet year and 1984 as a dry year [37].

127 As reference data for the model evaluation we use the Global Precipitation Climatology
 128 Center (GPCC) dataset [35] for precipitation, while the UDEL [43] is used for temperature.
 129 The Pearson's correlation coefficient (COR) is used to determine the skill of the model to
 130 simulate the variables pattern across the simulation period (Equation 2-1), the Root Mean
 131 Square Error (RMSE), (Equation 2-2) and the Mean Absolute Error (MAE), (Equation 2-3)
 132 are also calculated to assess the quality of the model and estimate model simulation biases:

$$133 \quad COR = \frac{cov(OBS, SIM)}{\sigma_{OBS} \cdot \sigma_{SIM}} = \frac{\sum_{i=1}^n (OBS_i - \overline{OBS})(SIM_i - \overline{SIM})}{\sigma_{OBS} \cdot \sigma_{SIM}} \quad \text{Equation 2-1}$$

$$134 \quad MAE = \frac{1}{n} \sum_{i=1}^n |SIM_i - OBS_i| \quad \text{Equation 2-2}$$

$$135 \quad RMSE = \sqrt{\frac{\sum_{i=1}^n (SIM_i - OBS_i)^2}{n}} \quad \text{Equation 2-3}$$

136 Where n is the number of sample, and OBS and SIM are the observed and simulated
 137 variables.

138 **2.4 Observational Datasets**

139 Based on availability throughout the study period (1980-2009), spatial resolution and
140 quality of data, the following sets are selected:

141 - The GPCP dataset version 6.0, covering the period 1901 to 2010, contains monthly
142 precipitation sums and has a spatial resolution of $0.5^\circ \times 0.5^\circ$ latitude by longitude [35].

143 - The University of Delaware (UDEL) monthly global dataset for air temperature and
144 precipitation from 1950 to 2010 with as spatial resolution of $0.5^\circ \times 0.5^\circ$ latitude by longitude
145 [43].

146 - The NCEP-LHF high resolution monthly mean global reanalysis dataset of the latent heat
147 flux, used as a proxy of evapotranspiration. The dataset is available from 1901 to 2015 at a
148 spatial horizontal resolution $0.3^\circ \times 0.3^\circ$ latitude by longitude [25].

149 **4. Results and Discussion**

150 We performed a Taylor diagram-based statistical analysis for the four model
151 configurations by comparing with the UDEL dataset for the monthly average temperature in
152 1999 and 1984. The analysis shows no significant difference between the chosen physics
153 packages, which indicates that the four parameterization groups behave similarly in
154 simulating the temperature over the Eastern Nile Basin (Figure 4 - A). Physics configurations
155 1 and 4 show nearly similar performance for both precipitation and temperature for the
156 selected two years (Figure 4 - B). However, as an overall an equally weighted average for the
157 RMSE and COR parameters for the selected 12 regions in the years 1984 and 1999, the
158 performance of physics configuration “4” was found to give slightly better results (Table 3)
159 and is selected for the historical 30 years downscaling experiment and includes “Lin” [9]
160 Microphysics scheme, “MYJ” [22] Planetary boundary layer parameterization scheme,
161 “BMJ” Cumulus scheme [23], “CAM” [12] radiation scheme and “NOAH” [8] land surface
162 model.

163 **3.1 Evapotranspiration**

164 The latent heat flux at the surface is a WRF output variable that can be used as an
165 indicator of evapotranspiration in terms of energy flux. The results of the model are compared
166 with the observational dataset NCEP-LHF for the 30-year simulation period from 1980 to
167 2009 to estimate the model bias shown in Figure 5, i.e. after conversion to the conventional
168 evapotranspiration unit (mm/day) using Equation 4-1. The model shows high precision in
169 simulating evapotranspiration in the region, with a relatively small bias that generally does
170 not exceed 0.5 mm/day.

$$171 \quad ET = \frac{LHF}{L_v} \quad \text{Equation 3-1}$$

172 where ET is the evapotranspiration in (mm/day), LHF is the latent heat flux in (W/m^2), L_v is
173 the latent heat of vaporization for water in (J/Kg).

174 **3.2 Temperature**

175 The 2-meter mean temperature over the 12 analysis sub-regions (Figure 6) shows a very
176 high correlation to the UDEL observational dataset. Figure 7-A also depicts the relatively
177 small temperature biases ($\pm 1^\circ C$), as expected [21,30], indicating that the simulated
178 temperature is adequate for the hydrologic applications.

179 **3.3 Precipitation**

180 Precipitation results from WRF are still highly uncertain due to the complexity of cloud
181 formation and the precipitation physics representation. The model appears to overestimate
182 precipitation over the highlands and underestimates it in low elevation regions, which needs
183 further validation for application in hydrologic applications. Figure 7-B shows the bias of the
184 daily average over the 30-year period from 1980 to 2009.

185 The bias in precipitation is evident in the comparison for sub-regions, showing an
186 underestimation in most of the dry parts and overestimation in the highlands, while both
187 overestimation and underestimation were noticed in some regions like in Obeid. Figure 8
188 illustrate the modeled precipitation over three regions (Akobo, BN and GERD) out of the 12-
189 selected analysis zones as time series of monthly precipitation (figures for other regions are
190 not shown), averaged over all grid points of each sub-region. Interestingly, substantial
191 differences between the monthly precipitations of the two gridded observational datasets are
192 also found. This underscores concerns regarding the uncertainty in observational data sets
193 [40].

194 The modeled precipitation is still subject to bias correction due to the obvious bias in
195 modeling the past/present compared to the GPCC and UDEL datasets. The following sections
196 will discuss in detail the correction methods followed, and the hydrologic verification
197 technique to assure the adequacy of the chosen correction method [16].

198 **3.4 Precipitation Bias Correction**

199 Several bias correction methods have been proposed, focusing mainly on precipitation
200 and temperature. In view of the intricacy of physical processes to simulate precipitation, there
201 are different methods at different levels of complexity available, from simple linear methods
202 to empirical or theoretical functions aiming to correct moments of precipitation distribution
203 [2].

204 Following a wide variety of bias correction methods [2], the algorithm followed to
205 correct the precipitation output of our climate simulations is based on verifying the adjusted
206 rainfall rates by applying them to a semi distributed Rainfall-Runoff hydrological model
207 (SWAT) and assessing the quality of the output flow hydrograph compared to that observed.

208 The aim is to ensure the adequacy of the corrected precipitation results for hydrologic
209 applications.

210 The selected study region for the SWAT model is the Gambella watershed, which is a part of
211 the Baro-Akobo-Sobat Sub-Basin of the EN as shown in Figure 9. The Gambella watershed
212 covers an area of approximately 23,450 km² over a wide elevation range, i.e. from a
213 minimum of 450 m to a maximum of 2,650 m. The watershed is calibrated using ground-
214 based observations of the runoff available near the streams in a previous study [34]. The
215 weather information used was from the global GHCN dataset version 2. After calibration, the
216 model has shown a very high coefficient of determination (R^2) value of nearly 0.95, and a
217 Nash-Sutcliffe Efficiency value (NSE) of 0.92.

218 The *First* bias-correction method is based on the probability distribution of the average
219 monthly precipitation in the whole domain [29]. The monthly GPCC precipitation is found to
220 be best fitted as Weibull distribution with a maximum likelihood method, and shape and scale
221 factors equal to 1.279 and 1.545, respectively, as shown in Figure 10 -A, while the modeled
222 precipitation has shape and scale factors equal to 1.202 and 1.183, respectively, as shown in
223 Figure 10 - B.

224 We find that the WRF simulated precipitation, i.e. according to the distribution
225 parameters, is underestimated by 30% compared to the observations, which is demonstrated
226 in the Q-Q plot of Figure 11 - A. The simulated precipitation is corrected by regressing the
227 simulated precipitation against the observation, resulting in a multiplicative constant so that
228 the Weibull distribution of the WRF precipitation becomes 1.242 and 1.539 for the shape and
229 scale factors, respectively, resulting in improved representation of the simulated precipitation,
230 and matching the observed GPCC precipitation over the EN region. The Q-Q plot of the bias-
231 corrected precipitation, shown in Figure 11 – B, gives the best representation of the
232 observations in the 30 years study period based on the probability distribution method.

233 The resulting bias-corrected precipitation is used as input for the SWAT hydrological
234 model for the Gambella watershed for verification. The runoff results of the hydrological
235 model shown in Figure 12-A yield a very high coefficient of determination ($R^2=0.88$), while
236 the values are highly overestimated according to the Nash-Sutcliffe Efficiency, about -0.15,
237 which is not acceptable for hydrological models. The bias-correction method based on the
238 probability distribution is therefore rejected for hydrological applications, even though the
239 statistical parameters indicate good agreement with observations.

240 The *Second* correction method relies on inspection of the precipitation bias against the
241 elevation in each grid as shown in Figure 13. The elevation contour lines are plotted over the
242 precipitation bias map for the 30-year period from 1980 to 2009. The bias is correlated to the
243 terrain elevation, notably over the ETH, such that the bias-correction algorithm is a function
244 of location and terrain elevation.

245 The bias-correction matrices are divided into five bands based on elevation ranges, with
246 band 1 representing the bias for grid points with elevation less than 500 m, band 2 from 500
247 to 1,000 m, band 3 from 1,000 to 1,500 m, band 4 from 1,500 to 2,000 m and band 5 for grids
248 of altitude more than 2,000 m as shown in Figure 14.

249 The bias is corrected using the GPCC dataset and applied to the WRF model output at a
250 condition that zero is the minimum value of precipitation. The resulting bias-corrected
251 precipitation is again coupled with the SWAT hydrological model for the Gambella
252 watershed. The runoff results of the hydrological model shown in Figure 12-B also yield a
253 high coefficient of determination ($R^2=0.80$) and a good Nash-Sutcliffe Efficiency of ~ 0.61 ,
254 which is considered sufficient for hydrological models.

255 The *Third* tested correction method is based on finding the relation between bias and the
256 time of the year as a repeating cycle throughout the considered period, with the same bias for
257 the same month, e.g. the monthly daily average precipitation bias from observations in

258 January 1980 was almost the same as in January 1981, 1982 ... etc. The algorithm of
259 correction depends on the daily average bias relative to the GPCC data in the same month,
260 across the year for each grid in the domain. Figure 15 depicts the generated 12 bias-correction
261 matrices as daily average bias in each month. It is clear that the bias in August is largest, with
262 an underestimation of more than 10 mm/day, and smallest in May, July and October, with
263 almost no precipitation prediction bias.

264 The-bias corrected precipitation is again coupled to the SWAT model for the Gambella
265 watershed to assess the correction method against the previous two methods. The runoff
266 results of the hydrological model, shown in Figure 12-C, yield a very high coefficient of
267 determination ($R^2=0.86$), and a very good Nash-Sutcliffe Efficiency (NSE) of ~ 0.79 , which is
268 considered excellent for hydrological models.

269 Hence, the three bias correction methods applied here resulted in statistically acceptable
270 results (overall mean and standard deviation of the modeled precipitation), however,
271 verification based on a hydrological model the results for runoff were different. The time-
272 location method was found to be the best bias-correction method, which should be applied to
273 the modeled precipitation output for use in hydrologic applications.

274 **5. Conclusions**

275 The WRF model appears to be able to achieve high precision in simulating both
276 temperature and evapotranspiration, with minor biases and errors based on the comparison
277 with the observational datasets. However, precipitation is less accurately simulated, and the
278 results need to be subject to bias correction to insure their validity for hydrologic
279 applications.

280 The three bias-correction methods applied to WRF simulated precipitation output
281 perform differently when compared to the rainfall-runoff hydrological model results. The
282 Time-Location method, assuming a repeating monthly bias cycle throughout the years over

283 the period considered appears to yield optimal performance, producing a valid precipitation
284 product for the EN region at a high resolution, appropriate for hydrologic applications. The
285 Time-Location method improved the NSE value of the runoff results using the WRF
286 corrected precipitation from -0.15 for the probability distribution correction method to 0.79,
287 as well as preserving the high coefficient of determination R^2 value around 0.86.

288 Hydrological verification of the bias-correction method is found to be an essential step in
289 approving the correction method, since the results need to be used in hydrologic applications.
290 Further, our results with the WRF model give confidence that scenario calculations will be
291 useful for the future projection of temperature, evapotranspiration and precipitation, the latter
292 at the condition of considering bias-correction with the proposed algorithm (Time-Location
293 Method). The success of this method also underscores the weakness of climate models in
294 reproducing rainfall in regions with pronounced topography.

295 **6. Acknowledgments**

296 *Sincere acknowledgements are due to Cairo University, The Cyprus Institute and Max*
297 *Planck Institute for Chemistry. Special acknowledgement is due to CORDEX for support*
298 *through training, computational resources and the professional technical assistance.*

299 **7. References and Citations:**

- 300 1. Argent, R. E. (2014). *Customization of the WRF Model Over the lake Victoria Basin*
301 *in East Africa*. North Carolina State University.
- 302 2. Argüeso, D., Evans, J. P., & Fita, L. (2013). Precipitation bias correction of very high
303 resolution regional climate models. *Hydrology and Earth System Sciences*, 17(11),
304 4379–4388. <http://doi.org/10.5194/hess-17-4379-2013>
- 305 3. Asore. (2012). *Impact of climate change on potential evapotranspiration and runoff*
306 *in the Awash River basin in Ethiopia*. Cairo University.

- 307 4. Berrisford, P., Dee, D. P., Poli, P., Brugge, R., Fielding, K., Fuentes, M., Simmons,
308 A. (2011, November). The ERA-Interim archive Version 2.0. *ERA Report Series*.
309 Shinfield Park, Reading: ECMWF.
- 310 5. Beyene, T., Lettenmaier, D. P., & Kabat, P. (2010). Hydrologic impacts of climate
311 change on the Nile River Basin: implications of the 2007 IPCC scenarios. *Climatic*
312 *Change*, *100*(3–4), 433–461. <http://doi.org/10.1007/s10584-009-9693-0>
- 313 6. Buontempo, C., Mathison, C., Jones, R., Williams, K., Wang, C., & McSweeney, C.
314 (2015). An ensemble climate projection for Africa. *Climate Dynamics*, *44*(7–8),
315 2097–2118. <http://doi.org/10.1007/s00382-014-2286-2>
- 316 7. Caldwell, P., Chin, H. N. S., Bader, D. C., & Bala, G. (2009). Evaluation of a WRF
317 dynamical downscaling simulation over California. *Climatic Change*, *95*(3–4), 499–
318 521. <http://doi.org/10.1007/s10584-009-9583-5>
- 319 8. Chen, F., Mitchell, K., Schaake, J., Xue, Y., Pan, H.-L., Koren, V., Betts, A. (1996).
320 Modeling of land surface evaporation by four schemes and comparison with FIFE
321 observations. *Journal of Geophysical Research*, *101*(D3), 7251.
322 <http://doi.org/10.1029/95JD02165>
- 323 9. Chen, S.-H., & Sun, W.-Y. (2002). A One-dimensional Time Dependent Cloud
324 Model. *Journal of the Meteorological Society of Japan*, *80*(1), 99–118.
325 <http://doi.org/10.2151/jmsj.80.99>
- 326 10. Clarke, L. E., Jacoby, H., Pitcher, H., Reilly, J., & Richels, R. (2007). Scenarios of
327 Greenhouse Gas Emissions and Atmospheric, (July), 154.
- 328 11. Cohen, S. J. (1990). Bringing the Global Warming Issue Closer to Home: The
329 Challenge Of Regional Impact Studies. *Bulletin of the American Meteorological*
330 *Society*. [http://doi.org/10.1175/1520-0477\(1990\)071<0520:BTGWIC>2.0.CO;2](http://doi.org/10.1175/1520-0477(1990)071<0520:BTGWIC>2.0.CO;2)

- 331 12. Collins, W. D., Rasch, P. J., Boville, B. A., Hack, J. J., McCaa, J. R., Williamson, D.
332 L., Zhang, M. (2006). The formulation and atmospheric simulation of the Community
333 Atmosphere Model version 3 (CAM3). *Journal of Climate*, 19(11), 2144–2161.
334 <http://doi.org/10.1175/JCLI3760.1>
- 335 13. DHI. (2006). *DHI product suite: Set of manuals: Water Atlas of the Blue Nile Sub-*
336 *Basin*. Denmark.
- 337 14. Di Baldassarre, G., Elshamy, M., van Griensven, A., Soliman, E., Kigobe, M.,
338 Ndomba, P., Uhlenbrook, S. (2011). Future hydrology and climate in the River Nile
339 basin: a review. *Hydrological Sciences Journal*, 56(2), 199–211.
340 <http://doi.org/10.1080/02626667.2011.557378>
- 341 15. Done, J. M., Leung, L. R., Davis, C. A., & Kuo, B. (2005). Regional Climate
342 Simulation Using the WRF Model . In *WRF/MM5 User's Workshop*.
- 343 16. Elshamy, M. E., Seierstad, I. A., & Sorteberg, A. (2009). Impacts of climate change
344 on Blue Nile flows using bias-corrected GCM scenarios. *Hydrology and Earth System*
345 *Sciences*, 13(5), 551–565. <http://doi.org/10.5194/hess-13-551-2009>
- 346 17. Evans, J. P. (2012). Regional Climate Modelling: The Future for Climate Change
347 Impacts and Adaptation Research. Retrieved April 5, 2016, from
348 [http://www.earthzine.org/2012/02/14/regional-climate-modelling-the-future-for-](http://www.earthzine.org/2012/02/14/regional-climate-modelling-the-future-for-climate-change-impacts-and-adaptation-research/)
349 [climate-change-impacts-and-adaptation-research/](http://www.earthzine.org/2012/02/14/regional-climate-modelling-the-future-for-climate-change-impacts-and-adaptation-research/)
- 350 18. Fujino, J., Nair, R., Kainuma, M., Masui, T., & Matsuoka, Y. (2006). Multi-gas
351 Mitigation Analysis on Stabilization Scenarios Using Aim Global Model. *The Energy*
352 *Journal*, 27, 343–353. Retrieved from <http://www.jstor.org/stable/23297089>
- 353 19. Gbobaniyi, E., Sarr, A., Sylla, M. B., Diallo, I., Lennard, C., Dosio, A., Lamptey, B.
354 (2014). Climatology, annual cycle and interannual variability of precipitation and

- 355 temperature in CORDEX simulations over West Africa. *International Journal of*
356 *Climatology*, 34(7), 2241–2257. <http://doi.org/10.1002/joc.3834>
- 357 20. Giorgi, F. (1990). Simulation of Regional Climate Using a Limited Area Model
358 Nested in a General Circulation Model. *Journal of Climate*, 3(9), 941–963.
359 [http://doi.org/10.1175/1520-0442\(1990\)003<0941:SORCUA>2.0.CO;2](http://doi.org/10.1175/1520-0442(1990)003<0941:SORCUA>2.0.CO;2)
- 360 21. IPCC. (2013). *CLIMATE CHANGE 2013 - The Physical Science Basis - Frequently*
361 *Asked Questions. CLIMATE CHANGE 2013 - The Physical Science Basis.*
- 362 22. Janjić, Z. I. (1990). The Step-Mountain Coordinate: Physical Package. *Monthly*
363 *Weather Review*, 118(7), 1429–1443. <http://doi.org/10.1175/1520->
364 [0493\(1990\)118<1429:TSMCPP>2.0.CO;2](http://doi.org/10.1175/1520-0493(1990)118<1429:TSMCPP>2.0.CO;2)
- 365 23. Janjić, Z. I. (1994). The Step-Mountain Eta Coordinate Model: Further Developments
366 of the Convection, Viscous Sublayer, and Turbulence Closure Schemes. *Monthly*
367 *Weather Review*, 122(5), 927–945. <http://doi.org/10.1175/1520->
368 [0493\(1994\)122<0927:TSMECM>2.0.CO;2](http://doi.org/10.1175/1520-0493(1994)122<0927:TSMECM>2.0.CO;2)
- 369 24. Jin, J., Miller, N. L., & Schlegel, N. (2010). Sensitivity Study of Four Land Surface
370 Schemes in the WRF Model. *Advances in Meteorology*, 2010(November), 1–11.
371 <http://doi.org/10.1155/2010/167436>
- 372 25. Kalnay, E., Kanamitsu, M., Kistler, R., Collins, W., Deaven, D., Gandin, L., Joseph,
373 D. (1996). The NCEP/NCAR 40-Year Reanalysis Project. *Bulletin of the American*
374 *Meteorological Society*, 77(3), 437–471. <http://doi.org/10.1175/1520->
375 [0477\(1996\)077<0437:TNYRPP>2.0.CO;2](http://doi.org/10.1175/1520-0477(1996)077<0437:TNYRPP>2.0.CO;2)
- 376 26. Kalognomou, E.-A., Lennard, C., Shongwe, M., Pinto, I., Favre, A., Kent, M.,
377 Büchner, M. (2013). A Diagnostic Evaluation of Precipitation in CORDEX Models
378 over Southern Africa. *Journal of Climate*, 26(23), 9477–9506.

- 379 <http://doi.org/10.1175/JCLI-D-12-00703.1>
- 380 27. Katragkou, E., García-Díez, M., Vautard, R., Sobolowski, S., Zanis, P., Alexandri, G.,
381 Jacob, D. (2015). Regional climate hindcast simulations within EURO-CORDEX:
382 evaluation of a WRF multi-physics ensemble. *Geosci. Model Dev.*, 8(3), 603–618.
383 <http://doi.org/10.5194/gmd-8-603-2015>
- 384 28. Laprise, R., Hernández-Díaz, L., Tete, K., Sushama, L., Šeparović, L., Martynov, A.,
385 Valin, M. (2013). Climate projections over CORDEX Africa domain using the fifth-
386 generation Canadian Regional Climate Model (CRCM5). *Climate Dynamics*, 41(11–
387 12), 3219–3246. <http://doi.org/10.1007/s00382-012-1651-2>
- 388 29. Legates, D. R., & McCabe, G. J. (1999). Evaluating the use of “goodness-of-fit”
389 Measures in hydrologic and hydroclimatic model validation. *Water Resources*
390 *Research*, 35(1), 233–241. <http://doi.org/10.1029/1998WR900018>
- 391 30. Legates, D. R., & Willmott, C. J. (1990). Mean seasonal and spatial variability in
392 global surface air temperature. *Theoretical and Applied Climatology*, 41(1–2), 11–21.
393 <http://doi.org/10.1007/BF00866198>
- 394 31. Lelieveld, J., Hadjinicolaou, P., Kostopoulou, E., Chenoweth, J., Maayar, M.,
395 Giannakopoulos, C., Xoplaki, E. (2012). Climate change and impacts in the Eastern
396 Mediterranean and the Middle East. *Climatic Change*, 114(3), 667–687.
397 <http://doi.org/10.1007/s10584-012-0418-4>
- 398 32. Mohamed, Y. A., van den Hurk, B. J. J. M., Savenije, H. H. G., & Bastiaanssen, W.
399 G. M. (2005). Hydroclimatology of the Nile: results from a regional climate model.
400 *Hydrol. Earth Syst. Sci.*, 9(3), 263–278. <http://doi.org/10.5194/hess-9-263-2005>
- 401 33. Otkin, J. A., H-L. Huang, and A. Seifert, (2006). A comparison of microphysical
402 schemes in the WRF model during a severe weather event. In *7th Annual WRF User’s*

- 403 *Workshop*. Boulder, CO, NCAR.
- 404 34. Raafat, A. (2015). *Assessment of the Impacts of Proposed Water Resources*
405 *Development Projects in Baro-Akobo-Sobat Basin on HAD*. Cairo University.
- 406 35. Schamm, K., Ziese, M., Becker, A., Finger, P., Meyer-Christoffer, A., Schneider, U.,
407 Stender, P. (2014). Global gridded precipitation over land: a description of the new
408 GPCP First Guess Daily product. *Earth Syst. Sci. Data*, 6(1), 49–60.
409 <http://doi.org/10.5194/essd-6-49-2014>
- 410 36. Shin, H. H., & Hong, S.-Y. (2011). Intercomparison of Planetary Boundary-Layer
411 Parametrizations in the WRF Model for a Single Day from CASES-99. *Boundary-*
412 *Layer Meteorology*, 139(2), 261–281. <http://doi.org/10.1007/s10546-010-9583-z>
- 413 37. Siam, M. (2010). *Impact of Climate Change on the Upper Blue Nile Catchment Flows*
414 *Using IPCC Scenarios*. Cairo University.
- 415 38. Skamarock, W.C. et al. 2008. “A Description of the Advanced Research WRF
416 Version 3.” *Technical Report (June)*: 113.
- 417 39. Soares, P. M. M., Cardoso, R. M., Miranda, P. M. A., Medeiros, J., Belo-Pereira, M.,
418 & Espirito-Santo, F. (2012). WRF high resolution dynamical downscaling of ERA-
419 Interim for Portugal. *Climate Dynamics*, 39(9), 2497–2522.
420 <http://doi.org/10.1007/s00382-012-1315-2>
- 421 40. Tanarhte, M., Hadjinicolaou, P., & Lelieveld, J. (2012). Intercomparison of
422 temperature and precipitation data sets based on observations in the Mediterranean
423 and the Middle East. *Journal of Geophysical Research: Atmospheres*, 117(D12),
424 <http://doi.org/10.1029/2011JD017293>
- 425 41. Tarabia, A. (2015). *Impact Assessment of the Proposed Water Resources*
426 *Development Projects in the Blue Nile Basin on Nile Flow at Aswan*. Cairo

427 University.

428 42. Tesemma, Z. (2009). Long Term Hydrologic Trends in the Nile Basin, (May), 83.

429 43. UDel. (2015). UDel_AirT_Precip data. Boulder, CO: NOAA/OAR/ESRL PSD.

430 Retrieved from <http://www.esrl.noaa.gov/psd/>

431 44. Weldemariam, H. G. (2015). *Dynamical Downscaling of GCM out puts to Determine*
432 *Impacts of Climate Change and Variability on the Hydrologic Sensitivity of Blue Nile*
433 *Basin Surface Water Resource Potential*. University of Nebraska.

434 45. Zittis, G., Hadjinicolaou, P., & Lelieveld, J. (2014). Comparison of WRF Model
435 Physics Parameterizations over the MENA-CORDEX Domain. *American Journal of*
436 *Climate Change*, 3(5), 490–511. <http://doi.org/10.4236/ajcc.2014.35042>

437 46. Zittis, G., Hadjinicolaou, P., & Lelieveld, J. (2016). Performance of WRF as a
438 regional climate model over the MENA-CORDEX domain; a comparison of two
439 radiation schemes. *International Journal of Climatology*.

440

441 **Tables:**

442 **Table 1.** WRF physics parameterization options tested in model sensitivity analyses

Physics	PH01	PH02	PH03	PH04
Microphysics	WSM6	Thompson	WSM6	LIN
Radiation Physics	CAM	CAM	CAM	CAM
Land Surface Model	NOAH	NOAH	NOAH	NOAH
Planetary Boundary Layer	MYJ	MYJ	YSU	MYJ
Cumulus scheme	BMJ	BMJ	BMJ	BMJ

443

444 **Table 2. Names and locations of the 12 sub-regions for analysis.**

#	Name	Longitude	Latitude	Region
		(Degrees East)	(Degrees North)	
1	Tana	37.2	12.0	Lake Tana
2	GERD	34.8	11.1	Grand Ethiopian Renaissance Dam
3	HAD	32.9	23.0	High Aswan Dam
4	Khartoum	32.5	15.5	Khartoum
5	Atbara	34.4	17.5	Atbara River
6	Sobat	34.5	8.5	Sobat River
7	Merowe	32.0	18.5	Merowe Dam
8	Tekeze	38.0	14.0	Tekeze
9	Akobo	34.0	6.0	Akobo River
10	BN	39.0	10.0	Blue Nile River
11	Pibor	33.2	4.5	Pibor
12	Obeid	29.0	13.0	Obeid

445

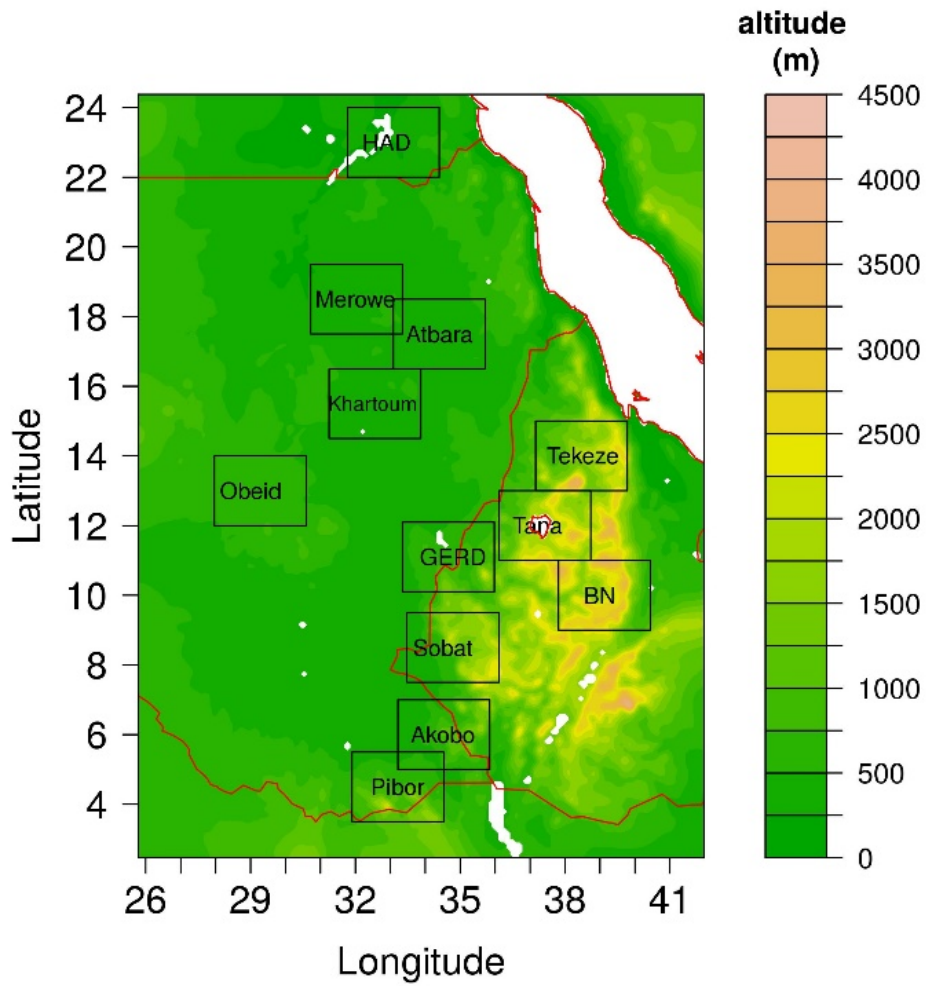
446 **Table 3. Comparison between Physics groups “1” and “4”.**

	Physics 1			Physics 4		
	RMSE	MAE	COR	RMSE	MAE	COR
Dry Year (1984)	0.73	1.29	0.5	0.68	1.24	0.49
Wet Year (1999)	1.0	1.15	0.47	0.96	1.09	0.5

447

448 **Figures:**

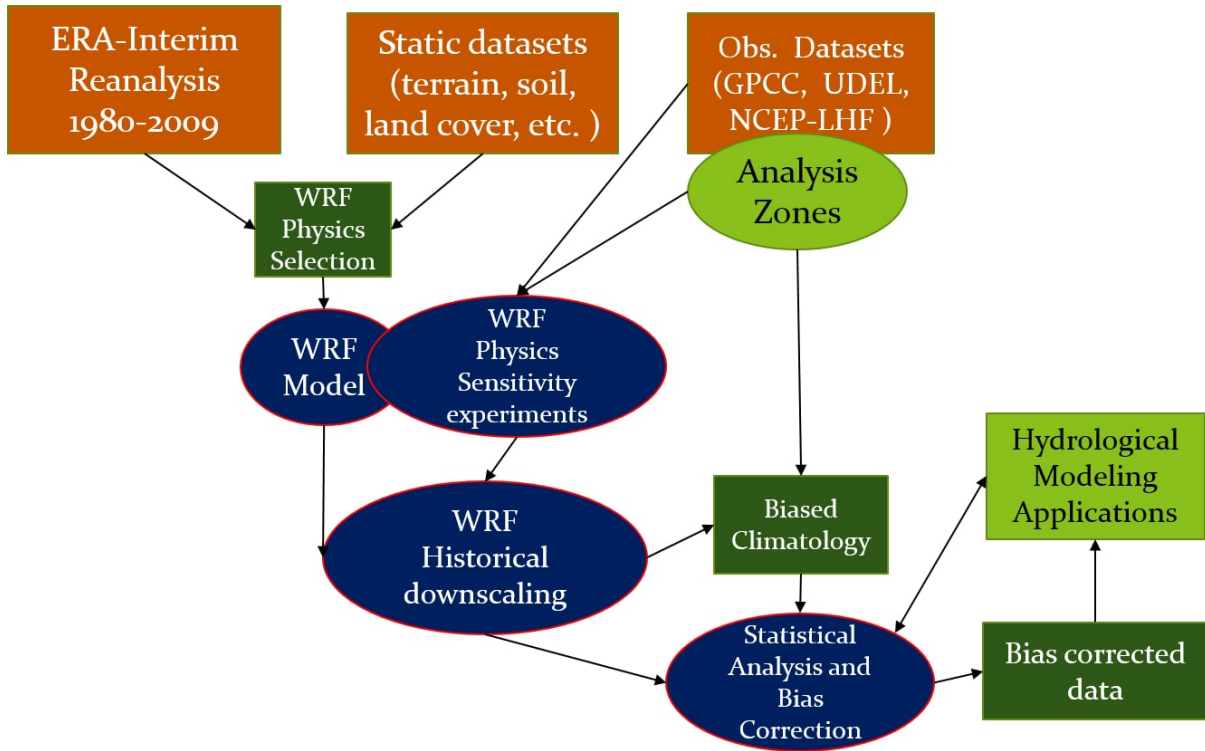
449



450

Figure 1. The Eastern Nile (EN) basin and sub-regions for evaluation

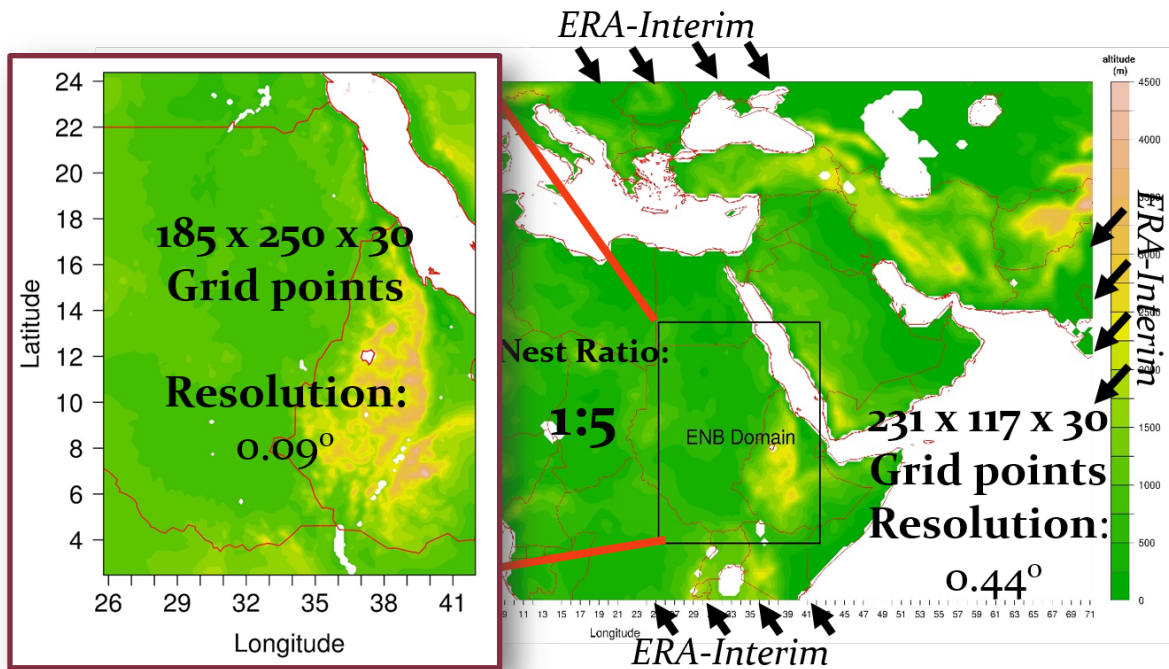
451



452

Figure 2. Methodology flow chart.

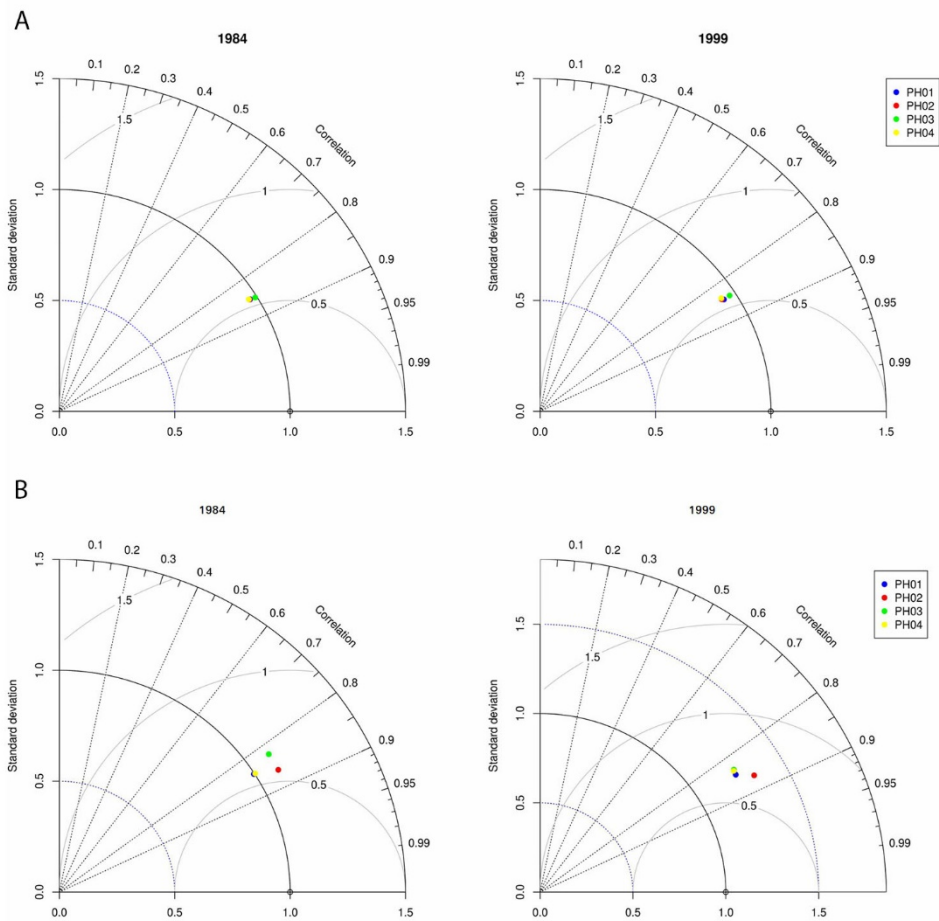
453



454

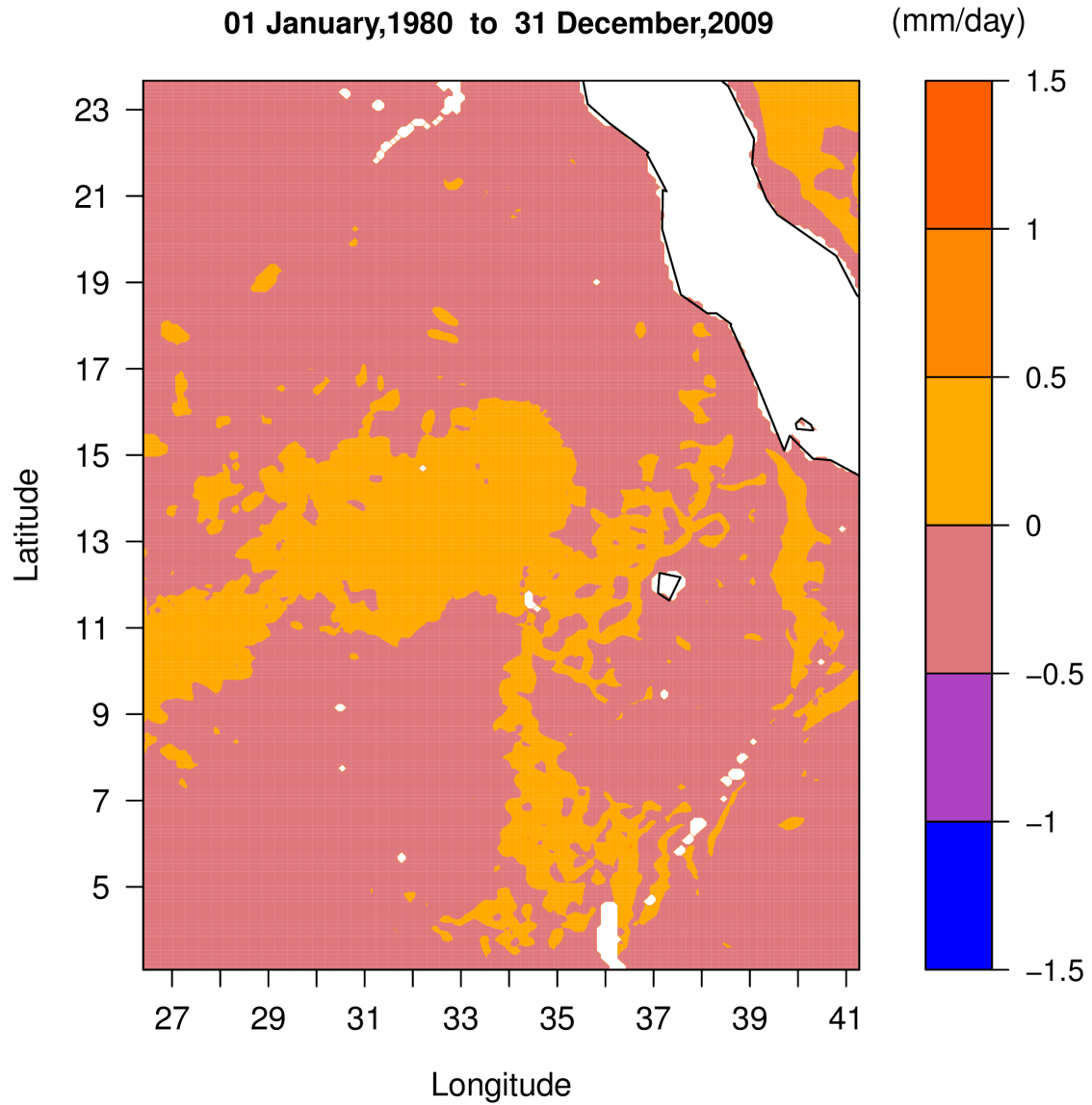
Figure 3. EN domain setup, nested within CORDEX MENA.

455



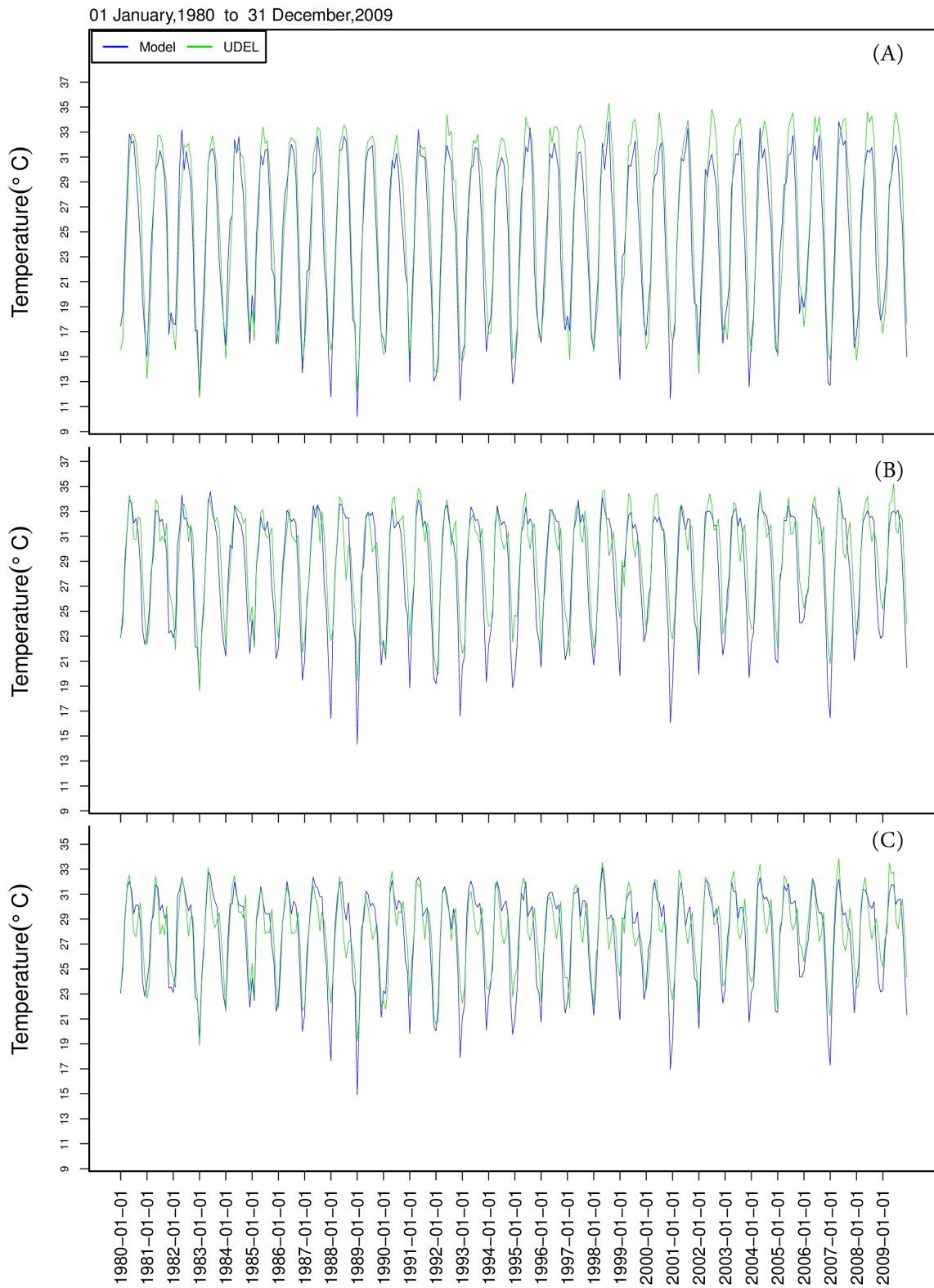
456 **Figure 4. (A) Taylor diagram for temperature over the EN basin for the four physics**
 457 **groups over the two test years, 1984 and 1999. (B) Taylor diagram for precipitation over**
 458 **the EN basin for the four physics groups over the two test years, 1984 and 1999.**

459



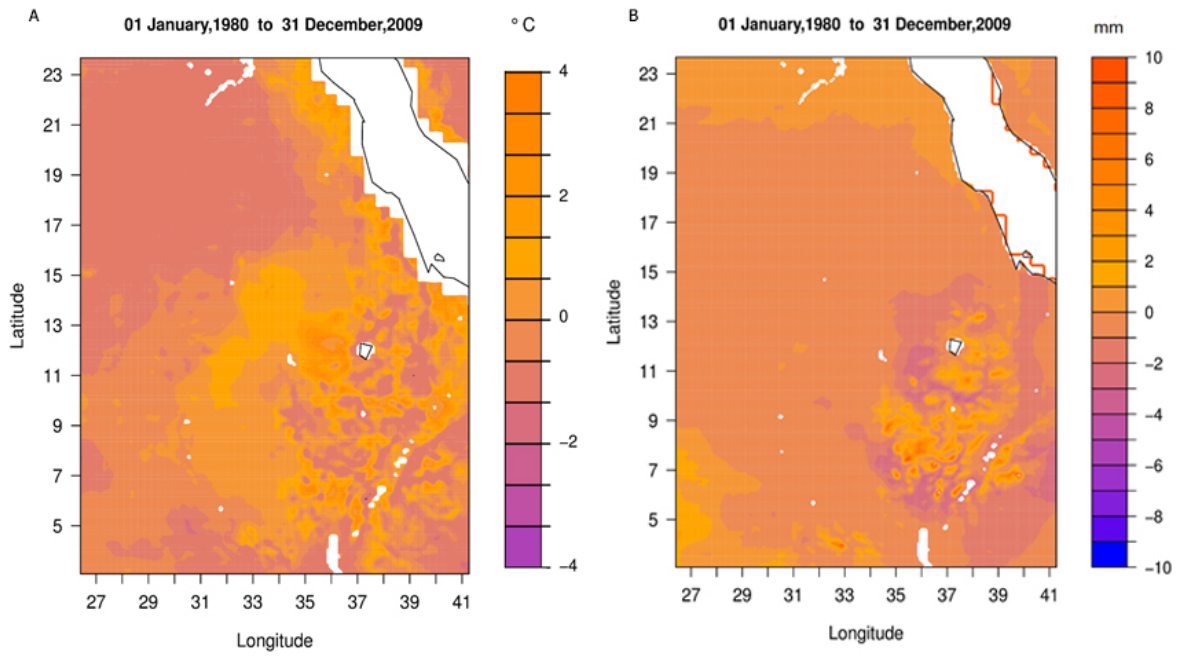
460 **Figure 5: WRF evapotranspiration, average daily bias from the NCEP-LHF dataset**
461 **between 1980 and 2009.**

462



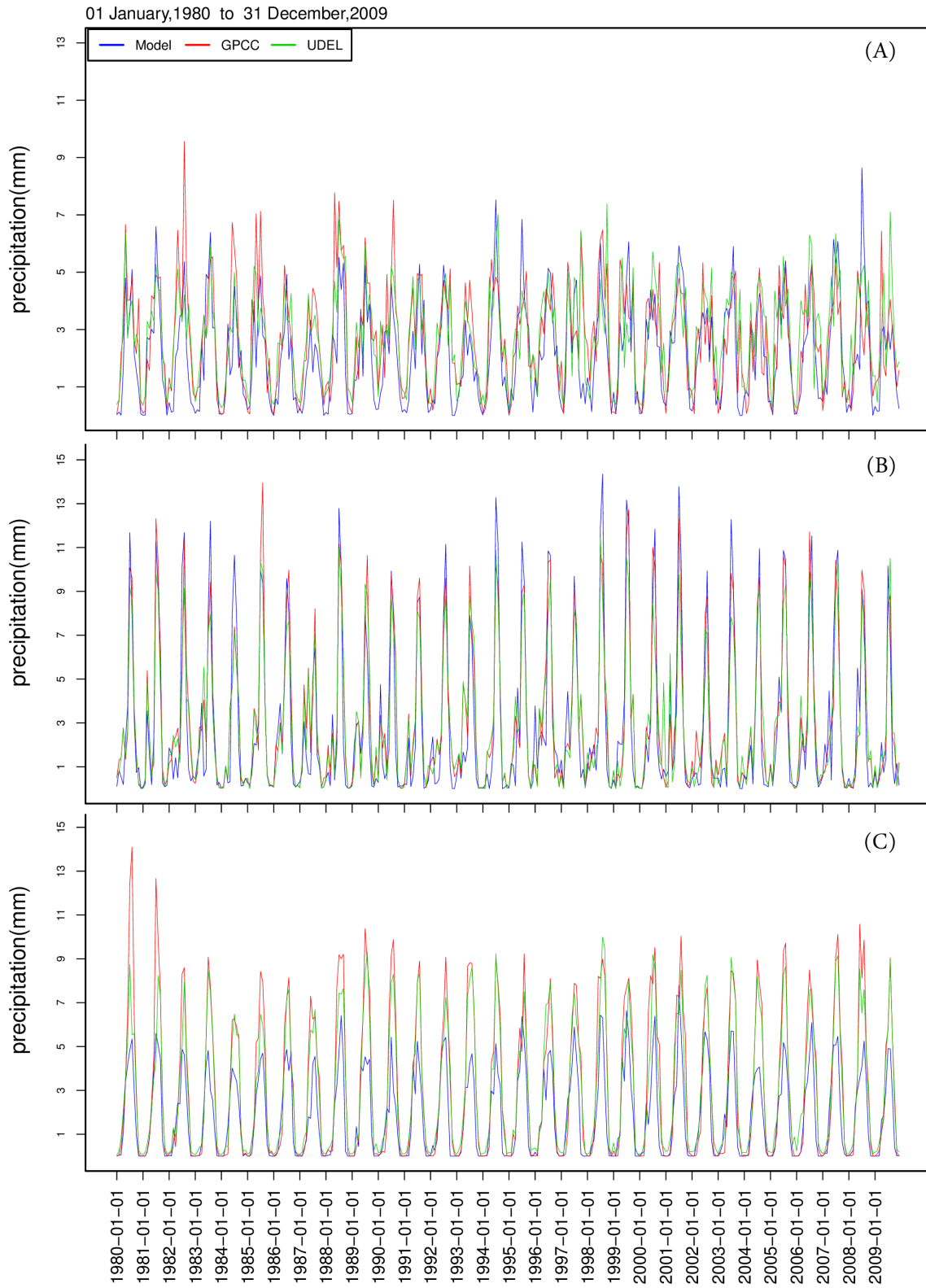
463 **Figure 6: WRF modeled temperature time series at: (A) HAD, (B) Khartoum and (C) Obeid.**

464



465 **Figure 7: (A) WRF modeled temperature bias compared to UDEL. (B) WRF modeled**
466 **precipitation bias compared to GPCC.**

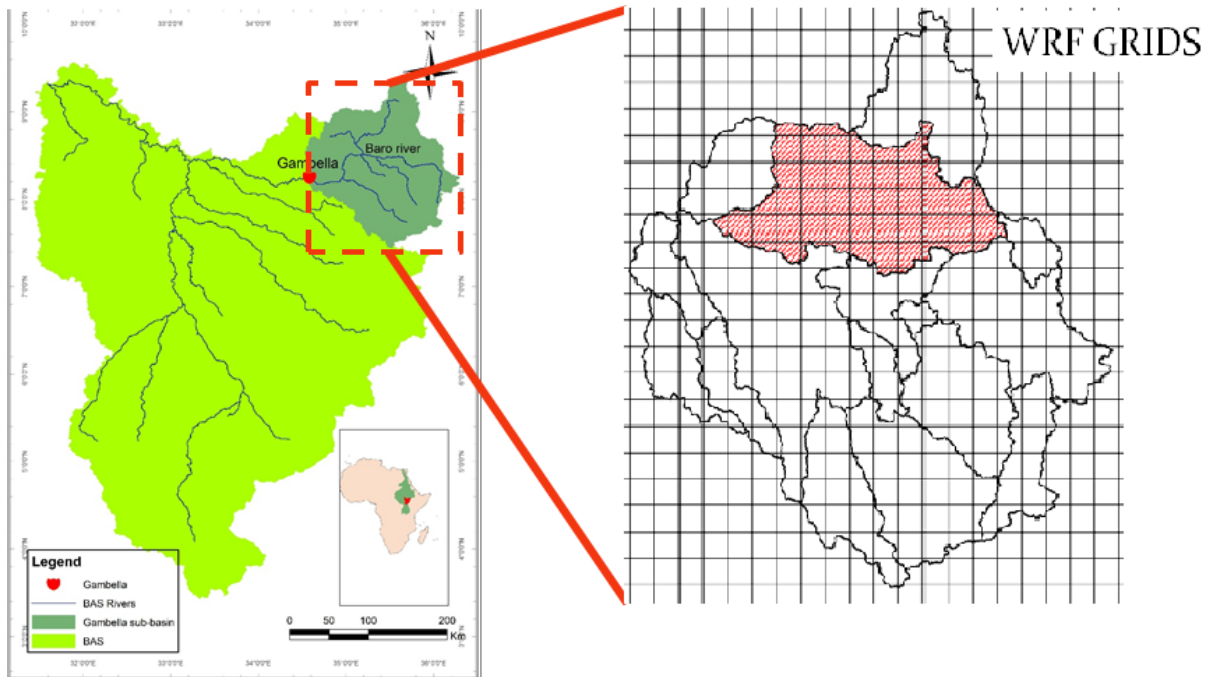
467



468

Figure 8: WRF modeled precipitation time series at: (A) Akobo, (B) BN and (C) GERD.

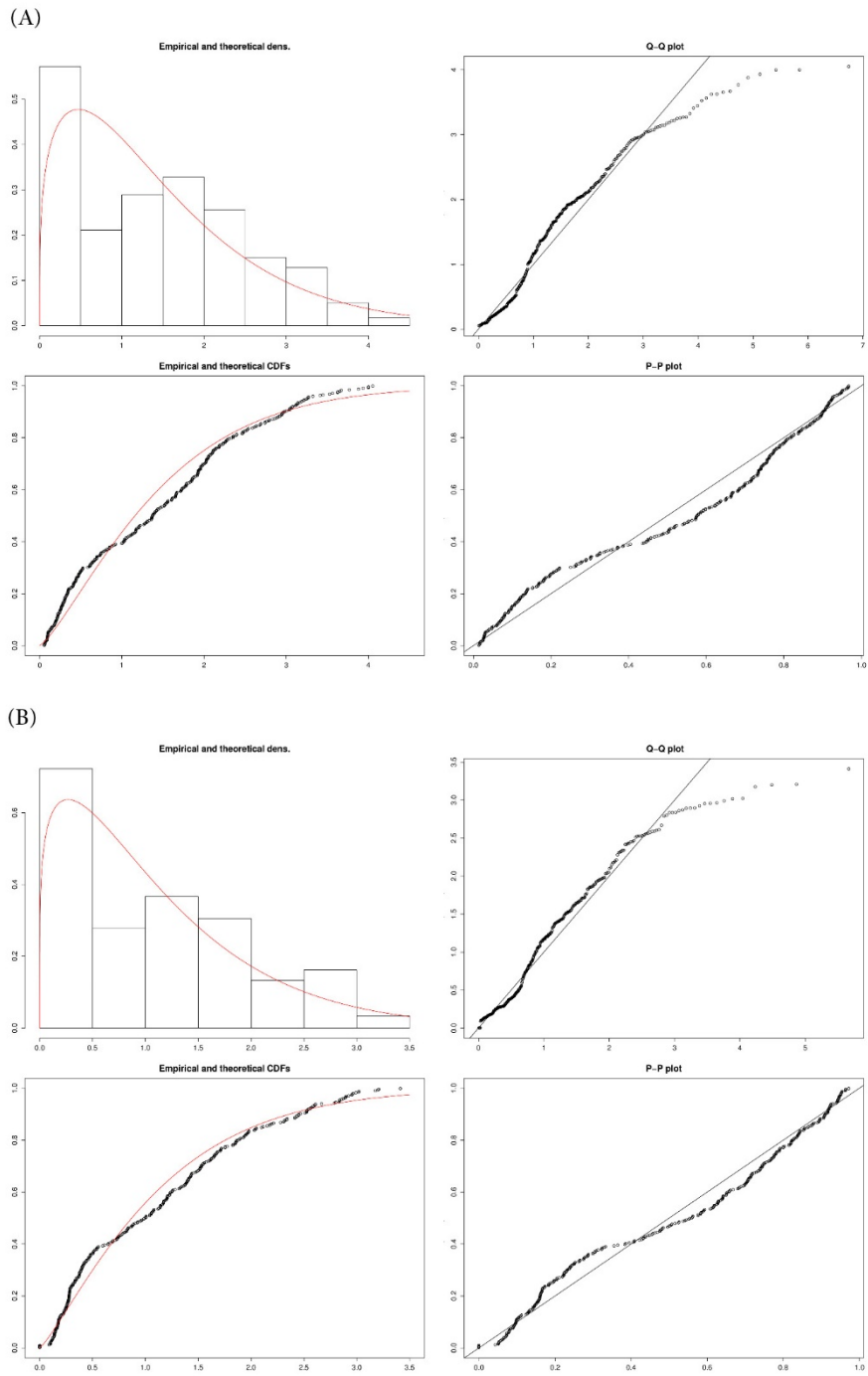
469



470
471

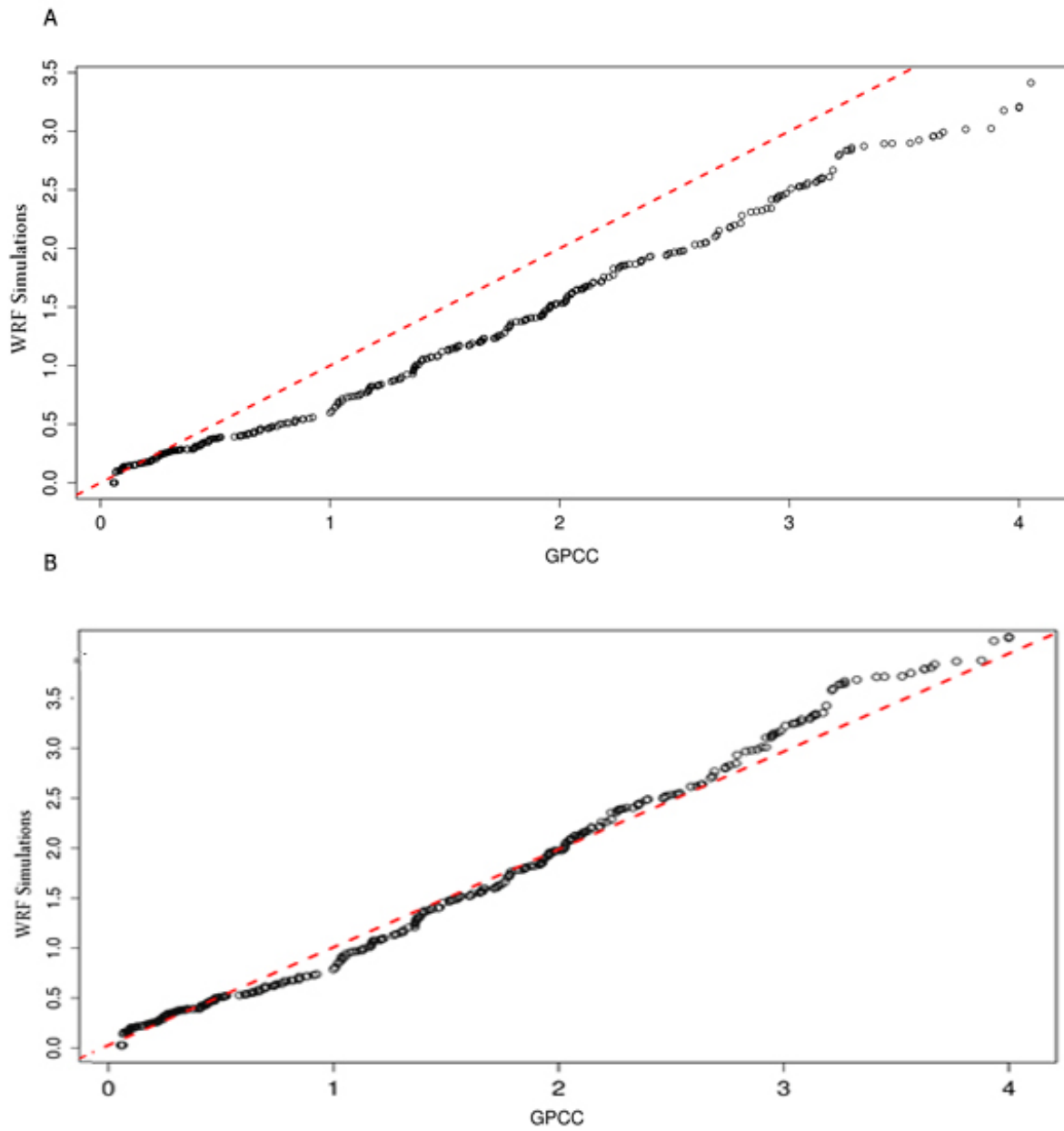
Figure 9: Gambella watershed location (left) and within the WRF model grid at a resolution of 0.09°x0.09° (right).

472



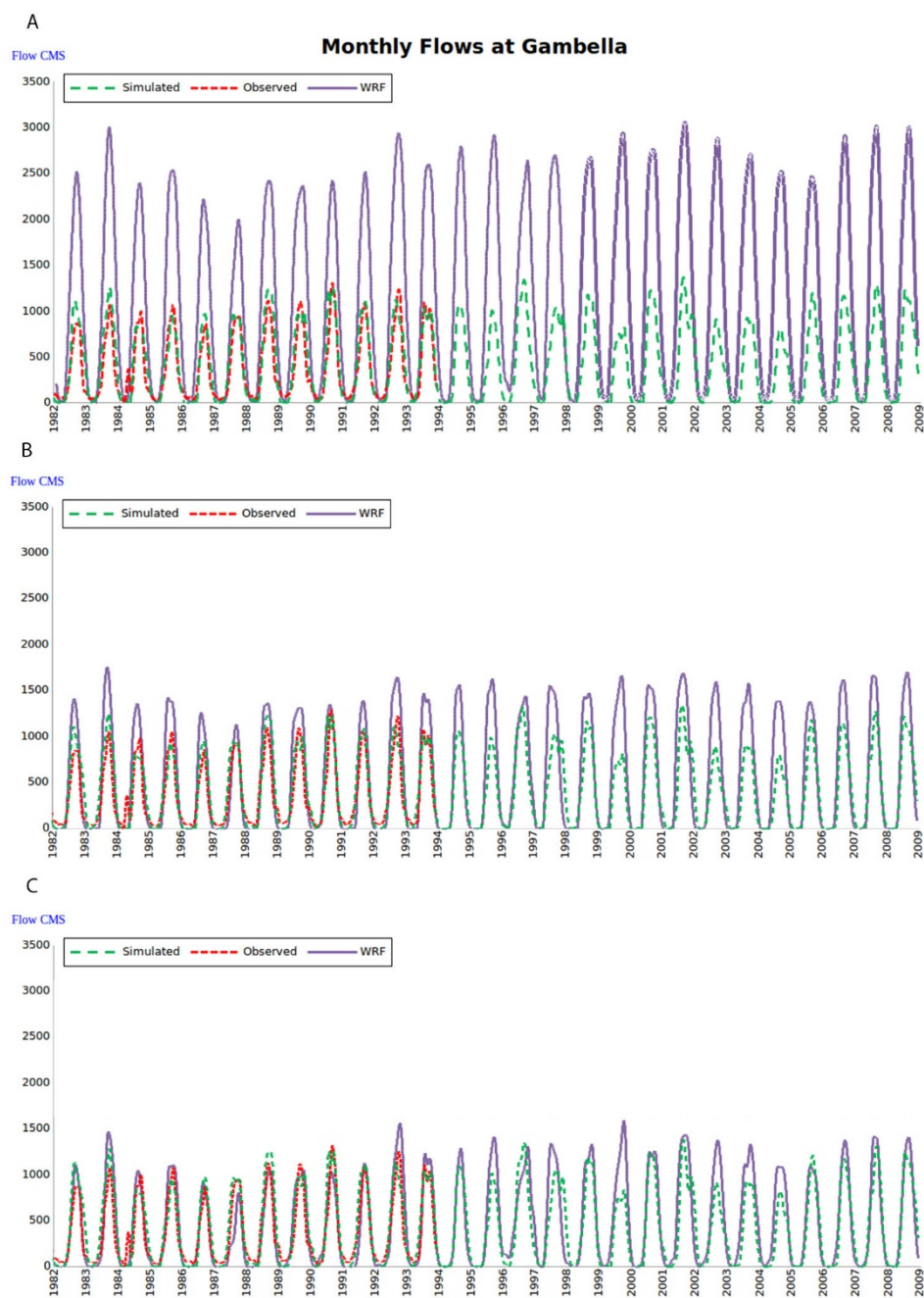
473 **Figure 10: (A) GPCCC precipitation Weibull distribution fitting. (B) WRF precipitation**
474 **Weibull distribution fitting.**

475



476 **Figure 11: (A) Q-Q plot for the modeled precipitation vs. the GPCC data. (B) Q-Q plot**
477 **for the bias-corrected simulated precipitation vs. the GPCC data.**

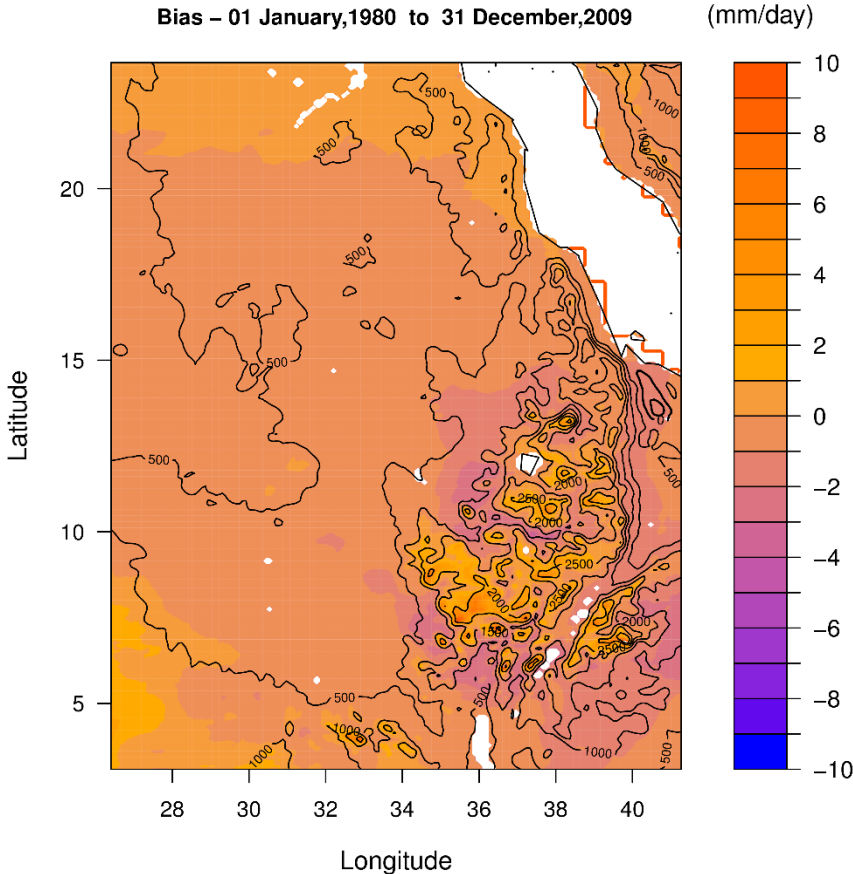
478



479 **Figure 12: Comparison of monthly flow at Gambella watershed between model forced**
 480 **by satellite data and WRF bias corrected precipitation: (A) probability distribution**
 481 **corrected, (B) Elevation-location corrected, (C) Time-location corrected.**

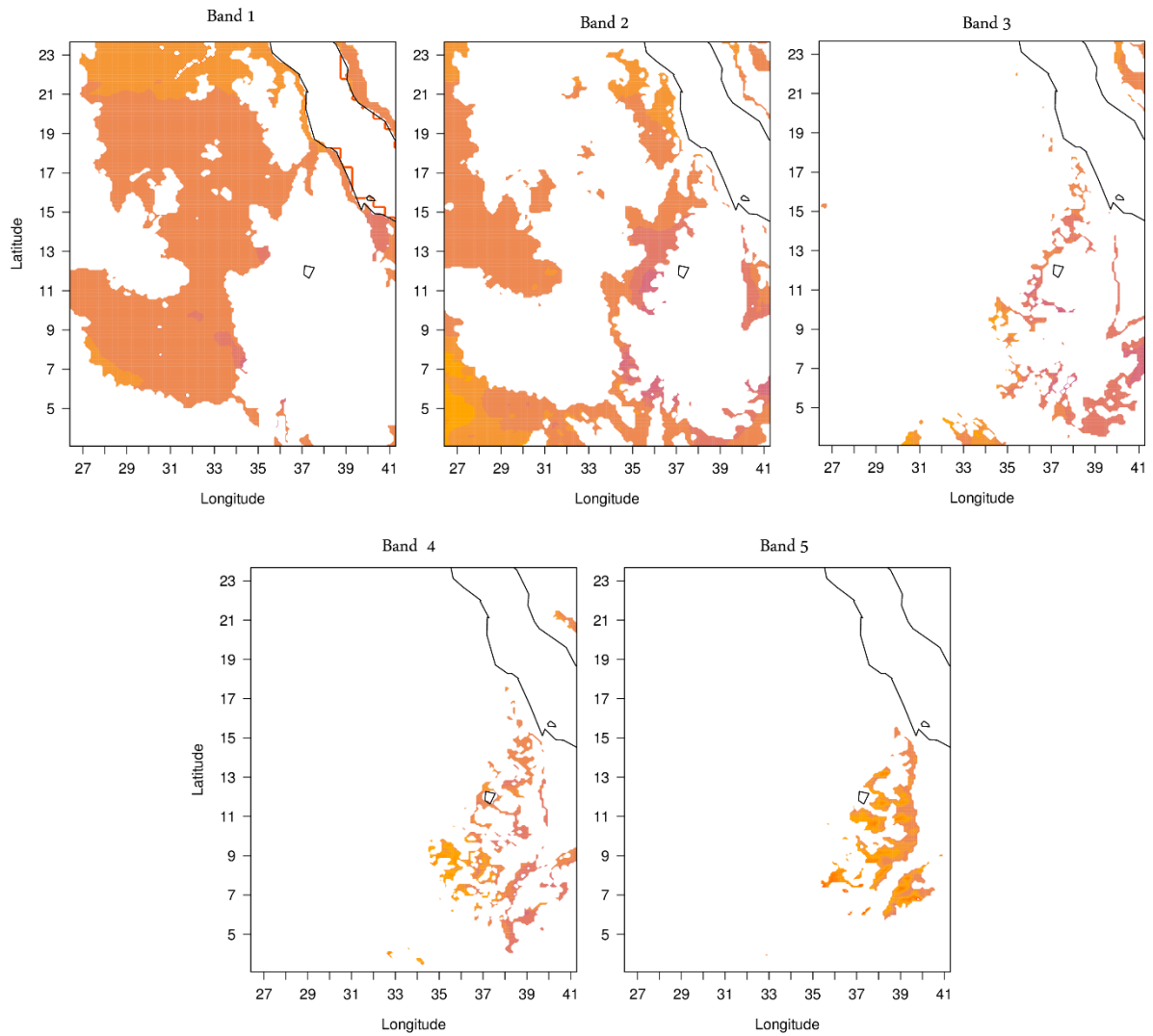
482

483



484 **Figure 13: WRF 30-year mean precipitation bias and terrain elevation contour lines.**

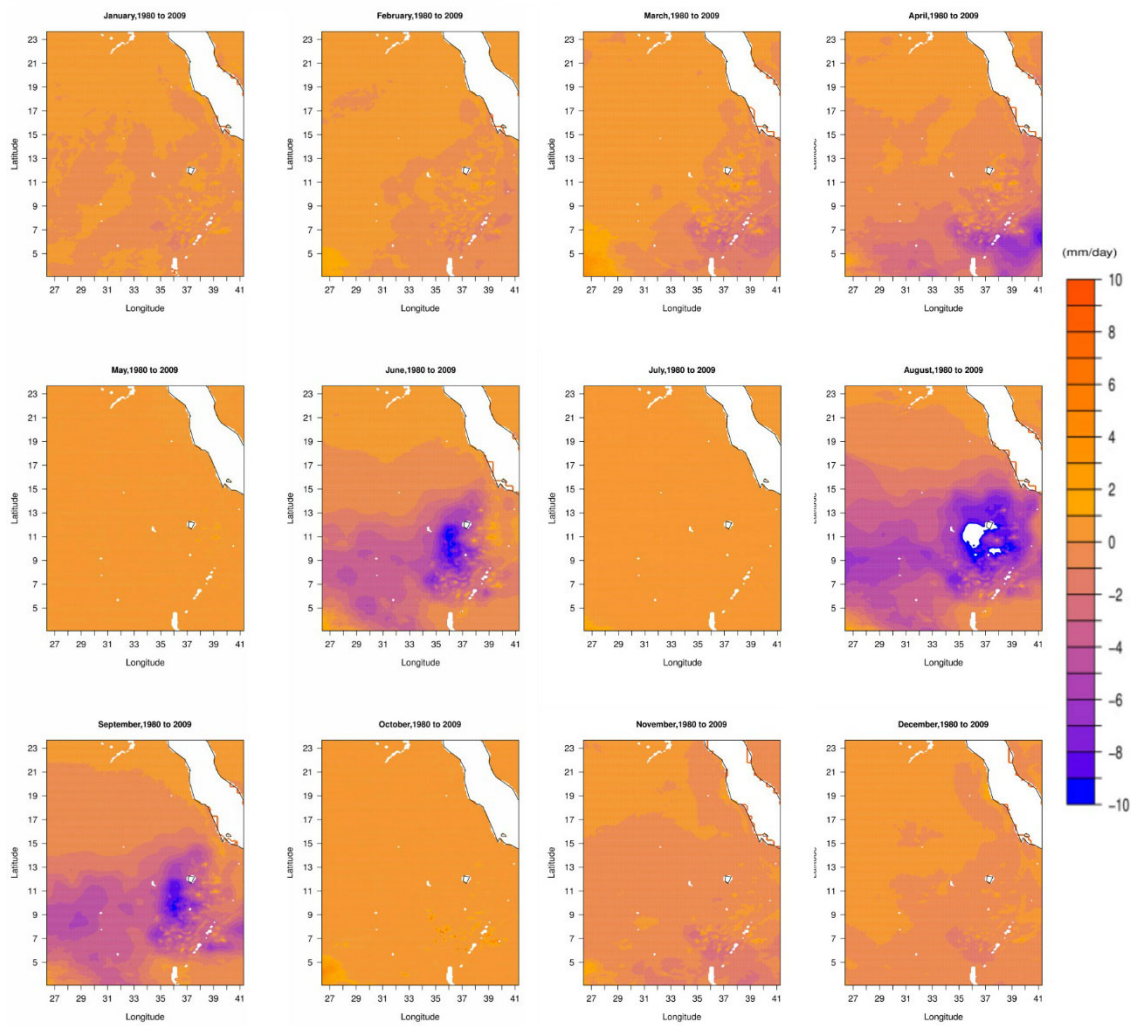
485



486

Figure 14: WRF precipitation bias in the five elevation bands.

487



488

Figure 15: Monthly time-location precipitation bias corrections.